Research Square

Preprints are preliminary reports that have not undergone peer review.
They should not be considered conclusive, used to inform clinical practice,
or referenced by the media as validated information.

Universal scaling and soft-mode limits of mass-neutral mechanical cloaking in architected lattices

Guangtao Wei

wgt@hrbeu.edu.cn

Fujian Agriculture and Forestry University https://orcid.org/0000-0001-8266-9776

Miao Yu

Fujian Agriculture and Forestry University

Jun Liu

Fujian Provincial Cancer Hospital

Research Article

Keywords:

Posted Date: November 25th, 2026

DOI: https://doi.org/10.21203/rs.3.rs-11850449/v1

License: This work is licensed under a Creative Commons Attribution 4.0 International License.
Read Full License

Additional Declarations: The authors declare no competing interests.

Universal scaling and soft-mode limits of mass-neutral mechanical cloaking in architected lattices

Guangtao Wei[1,*], Miao Yu[1], Jun Liu[2,*]

[1] College of Mechanical and Electrical Engineering, Fujian Agriculture and Forestry University, Fuzhou 350002, Fujian, China.

[2] Department of Medical Oncology, Clinical Oncology School of Fujian Medical University, Fujian Cancer Hospital, Fuzhou 350000, Fujian, China.

*Corresponding authors: Guangtao Wei (e-mail: wgt@hrbeu.edu.cn); Jun Liu (e-mail: 344196244@qq.com).

Abstract

Circular openings sever continuous axial load paths in architected lattices that are stiff in compression yet compliant in shear (stiffness ratio ~24–100). Across 19 homogenizable Laguerre lattices, we find that bare-hole shear-to-axial visibility collapses onto the universal law $\Delta_\gamma/\Delta_\varepsilon \approx 3.4/\lambda$, where $\lambda = \sqrt{C_{11}C_{22}}/C_{66}$ ($r^2 = 0.97$), in agreement with anisotropic Lekhnitskii dipole theory ($r^2 = 0.986$). Exploiting this separation of axial and shear channels, spatially grading strut and joint-neck widths within unmodified square-lattice connectivity, exact mass neutrality, and additive-manufacturing feature bounds routes axial load laterally around the void, cutting worst-case platen displacement mismatch by 44% ($J = 0.559$) while outperforming the bare hole across all eight held-out continuum loads and virtual manufacturing scatter realizations ($\sigma_\mathrm{b} = 0.06$ mm). Equal-mass packing requires $r_\mathrm{cloak} \gtrsim 1.6\, r_\mathrm{void}$, with gains saturating over ~2.4 cell pitches, enabling a 36-entry width table to recover 54–82% of re-optimized performance without re-optimization. Finally, a fiber-limit theory governed by $\xi = a\sqrt{\lambda}/H$ and ring exponent m_eff predicts platen-trained soft-mode bias within 1.3× across seven of eight topologies, identifies self-suppression in the high-Poisson 4.8.8 lattice ($r_\mathrm{s} = 0.619$), and reveals from 25-dimensional operator spectra that reducing peak error at low density can cut random-load pass rates from 60.4% to 5.2%.

Introduction

Structural openings—such as access ports, cable passages, fastener holes, and inspection windows—are unavoidable in load-bearing components and generate long-range stress and displacement disturbances in continuous elastic sheets [1, 2]. Mansfield [3] showed that a profiled reinforcement around a cutout can render an opening mechanically neutral, restoring the exact exterior stress field of an uncut plate under a targeted remote stress state, although neutrality under one loading mode generally breaks down under another. Subsequent theoretical advances generalized neutrality to coated inclusions and tailored elastic interfaces in composite media [4–6]. Extending this paradigm toward arbitrary external loads was later formalized as elastic cloaking by analogy with coordinate-transformation optics [7]. However, Milton, Briane, and Willis [8] proved that linear elasticity is not form-invariant under general coordinate mappings, implying that exact transformation cloaking requires generalized Cosserat or Willis-type constitutive couplings [9]. Practical approximations have therefore been realized across in-plane elastic media [10], flexural plates [11, 12], pentamode and bimode metamaterials [13–16], and coordinate-warped lattices [17, 18].

To circumvent restrictive coordinate transformations, inverse-design strategies optimize geometry directly to minimize exterior displacement mismatch building upon classical structural and topology optimization [19, 20]. Notable demonstrations include optimized truss-lattice cloaks [21], data-driven aperiodic metamaterials [22], concurrent multiscale and compatible-boundary topology optimization [23–25], disordered cellular architectures

[26], and minimax unbiased design of spinodal metamaterials [27]. Crucially, Senhora et al. [27] demonstrated that cloaks trained solely on a small fixed set of axial loads risk behaving merely as load-specific reinforcements unless rigorously audited against unseen multi-axial, shear-dominated, and non-affine boundary displacement fields. Yet whether such multi-load unbiasedness can be enforced in strongly anisotropic lattices without sacrificing primary uniaxial cloaking performance—or triggering hidden error redistribution across the remaining boundary-load spectrum—has remained unresolved.

Architected cellular materials and periodic lattices introduce an additional microstructural challenge absent from isotropic continua [28–30]: macroscopic elastic response is governed strongly by nodal connectivity and member geometry [31, 32]. A regular square lattice, for instance, is stretching-dominated along its two orthogonal principal axes yet bending-dominated in in-plane shear, so axial stiffness scales linearly with relative density $\overline{\rho}$ whereas shear stiffness scales as $\overline{\rho}^3$ [33]. Cutting a circular hole severs continuous axial columns and creates a long-range disturbance channeled along the loaded direction, whereas in-plane shear deforms members by gentle joint bending and leaves the hole nearly invisible. An effective lattice cloak must therefore restore interrupted axial load paths along both orthogonal axes without excessively stiffening the surrounding annulus in shear—a requirement directly opposed by coordinate-transformed lattices that curve straight columns into compliant bending arcs. Engineering deployment further imposes three practical constraints: exact mass neutrality relative to the intact plate, shared connectivity and additive-manufacturing feature bounds with the host lattice, and rapid scale transfer across opening dimensions without repeating full numerical optimization.

Here, we resolve this trade-off across architected lattices while holding background connectivity, intact solid area, and selective-laser-sintering (SLS) fabrication bounds strictly invariant, verifying every metric on high-resolution continuum finite-element meshes (Methods). Five quantitative findings establish the governing mechanics of lattice cloaking. First, across 19 homogenizable Laguerre and Archimedean lattices, bare-hole shear-to-axial visibility collapses onto the universal law $\Delta_\gamma/\Delta_\varepsilon \approx 3.4/\lambda$ ($r^2 = 0.97$), matching anisotropic Lekhnitskii dipole theory ($r^2 = 0.986$). Second, purely grading strut and compliant joint-neck widths diverts axial loads laterally around the opening, cutting worst platen mismatch by 44% ($J = 0.559$) while beating bare holes across all eight held-out continuum loads and ten paired width-scatter realizations ($\sigma_\mathrm{b} = 0.06$ mm) and surpassing every equal-mass homogeneous non-auxetic continuum ring. Third, area conservation imposes the packing threshold $r_\mathrm{cloak} \gtrsim 1.6\, r_\mathrm{void}$, above which gains saturate over one shear-lag transfer length ($\Lambda_\mathrm{min} \approx 2.4\, \ell$) and transfer across sizes via a 36-entry width lookup table. Fourth, a fiber-limit model governed by $\xi = a\sqrt{\lambda}/H$ and ring stiffness exponent m_eff predicts platen-trained soft-mode bias within 1.3× across seven of eight topologies, uncovers self-suppression under frictionless uniaxial training in the high-Poisson Archimedean 4.8.8 lattice ($r_s = 0.619$), and reveals via 25-dimensional operator spectra that suppressing peak excess at $\overline{\rho} = 0.25$ can reduce the random-load pass rate from 60.4% to 5.2%.

Results

Universal bare-hole visibility collapse across 19 architected lattices

Before designing an insert, we first establish why circular cutouts produce radically different exterior signatures across lattice architectures. For slender, rigid-jointed struts of base modulus E_s at relative density $\overline{\rho}$, a regular square lattice possesses effective axial modulus $E = E_s\overline{\rho}/2$, near-zero Poisson's ratio $\nu \approx 0$, and bending-dominated shear modulus $G = E_s\overline{\rho}^3/16$ [28, 34], generating extreme elastic anisotropy:

$$\kappa_\square = \frac{E}{G} = \frac{8}{\overline{\rho}^2} \approx 65 \quad (\overline{\rho} = 0.35) \tag{1}$$

By contrast, an equilateral triangular lattice is stretching-dominated in both tension and shear ($\kappa = 2.7, \nu = 1/3$), a hexagonal honeycomb is nearly isotropic and bending-dominated ($\kappa \approx 3.6$), and bracing the square lattice with both diagonals cuts anisotropy to $\kappa \approx 2.0$ ($\nu \approx 0.41$). In Lekhnitskii's anisotropic elasticity formalism [35], the characteristic equation $\mu^4 + \kappa\mu^2 + 1 = 0$ yields roots $\mu \approx i/\sqrt{\kappa}, i\sqrt{\kappa}$, implying that an axial disturbance around a cutout of radius a channels along principal columns over an anisotropic decay distance $a\sqrt{\kappa} \approx 8a > L$, exceeding the entire plate width. Direct beam and homogenized plane-stress comparisons under 1% uniform strain on all four edges confirm this contrast (Supplementary Table S6): for the reference $\overline{\rho} = 0.35$ square lattice, uniform axial strain ε_{yy} generates 10.7% (beam) and 9.5% (continuum) exterior displacement error around VOID, whereas pure shear γ_{xy} generates only 0.54% and 0.43% error—corresponding to shear-to-axial visibility ratios of just 0.050 and 0.046. In isotropic triangular and braced-square lattices, shear and axial errors remain nearly equal (ratios 1.19/1.12 and 0.87/1.30), while honeycombs sit at intermediate ratios (0.31/0.22).

For an infinite orthotropic sheet with $\nu = 0$, Lekhnitskii's far-field dipole expansion (Methods) yields an exact closed-form analytical expression for the shear-to-axial hole visibility ratio:

$$\frac{\Delta_\gamma}{\Delta_\varepsilon} = \frac{2(q+2)}{\kappa}\sqrt{\frac{q^2+1}{q^4+2q^3+q^2+2q+4}}, \quad q = \sqrt{\kappa+2}, \quad \frac{\Delta_\gamma}{\Delta_\varepsilon} \to \frac{2}{\kappa}\left(1+\kappa^{-1/2}\right) \ (\kappa \gg 1) \tag{2}$$

Equation (2) evaluates to $0.034, 0.025, 0.99, 0.73$, and 1.35 across the five benchmark backgrounds in Supplementary Table S6—and to $0.034, 0.025, 1.05, 0.24$, and 1.35 when the full nonzero-ν dipole formulation is retained—spanning nearly two orders of magnitude. To test whether a single elastic invariant governs bare-hole visibility across arbitrary cellular geometries, we screened 63 periodic and Archimedean tilings [36] alongside disordered Laguerre Voronoi cellular networks [37, 38] at uniform relative density $\overline{\rho} = 0.30$. Forty-one candidates failed geometric connectivity or minimum-clearance gates prior to mechanical homogenization, leaving 22 connected periodic graphs; applying a central-window affine-strain homogenization test (Methods) removed three strongly non-affine outliers whose interior strain departs by $> 50\%$ (specifically 82–97%; Supplementary Figs. S9, S10 and Supplementary Table S19).

Across the 19 homogenizable backgrounds, plotting $\Delta_\gamma/\Delta_\varepsilon$ against the engineering stiffness ratio $\kappa = \sqrt{E_1 E_2}/G_{12}$ splits the data into two distinct Poisson branches and achieves only modest correlation ($r^2 = 0.73$, Fig. 1a). Replacing κ with the strain-controlled stiffness ratio $\lambda = \sqrt{C_{11}C_{22}}/C_{66} = \kappa/(1-\nu^2)$, however, collapses all 19 printable and mechanics-only topologies onto a single universal scaling curve $\Delta_\gamma/\Delta_\varepsilon \approx 3.4/\lambda$ (log–log slope -0.97, $r^2 = 0.97$, Fig. 1b). Why does $\lambda = \sqrt{C_{11}C_{22}}/C_{66}$ rather than κ serve as the universal scaling variable? At fixed macroscopic shear strain, transverse expansion enters the strain energy exclusively through off-diagonal stiffness terms, whereas uniaxial engineering definitions mix Poisson expansion into both numerator and denominator. Consequently, full-tensor anisotropic dipole predictions calculated directly from the measured intact stiffness tensors $\boldsymbol{C}$ match continuum finite-element visibility across nearly two decades ($r^2 = 0.986$, Fig. 1c). Crucially, this scaling reflects bulk constitutive anisotropy rather than circular symmetry alone: equal-area 2:1 elliptical and rounded-square holes oriented at 0° and 45° obey the same inverse law with modest shape prefactors $2.9–3.7$ ($r^2 = 0.97–0.99$, Fig. 1d). Furthermore, sweeping relative density in the square lattice ($\overline{\rho} = 0.25–0.45$) yields continuum unit-cell ratios $\lambda_{\text{cont}} \in \{99.7, 66.8, 45.7, 32.4, 23.9\}$ that capture finite nodal-hub stiffening in non-slender lattices [39] and collapse bare-hole visibility onto $3.0/\lambda_{\text{cont}}$ within $1–6\%$. Extending the dipole analysis to spherical cavities in three-dimensional cubic elastic media reveals an analogous inverse scaling $\Delta_\gamma/\Delta_\varepsilon \approx 2.8/\lambda_3$ (Supplementary Fig. S8a), establishing a unified dimensional scaling principle across two- and three-dimensional anisotropic cellular solids.

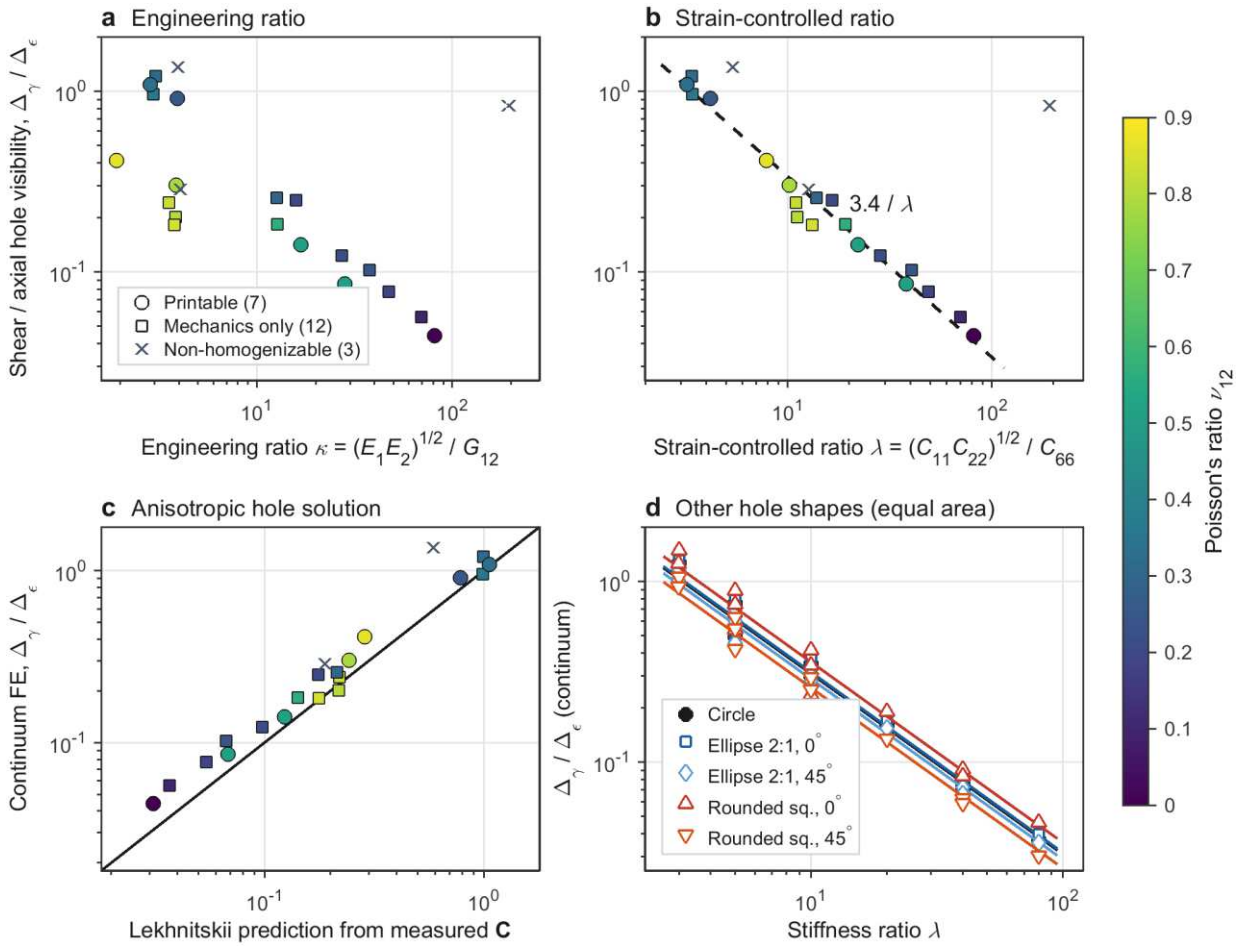

Fig. 1 | Universal bare-hole visibility collapse across 19 architected lattices. a, Measured shear-to-axial exterior mismatch ratio $\Delta_\gamma/\Delta_\varepsilon$ versus engineering stiffness ratio κ (continuum h = 0.1 mm, 1% uniform strain), showing separation by Poisson's ratio ν_{12}. Circles denote printable architectures (7), squares denote mechanics-only connected networks (12), and crosses mark three excluded non-homogenizable outliers. **b**, Collapse onto the single master curve $\Delta_\gamma/\Delta_\varepsilon \approx 3.4/\lambda$ ($r^2 = 0.97$) using the strain-controlled ratio $\lambda = \sqrt{C_{11}C_{22}}/C_{66}$. **c**, Parity between continuum finite-element (FE) visibility and full anisotropic Lekhnitskii dipole predictions from homogenized stiffness tensors (Methods; complete 22-network library in Supplementary Fig. S9 and Supplementary Table S19). **d**, Persistence of A/λ scaling across equal-area elliptical (2:1) and rounded-square holes at $0^\circ, 45^\circ$ ($A = 2.9–3.7$, $r^2 = 0.97–0.99$).

Mass-neutral width grading and lateral load bypass

Because circular openings in square lattices distort exterior fields primarily by interrupting axial columns while shear remains nearly unperturbed, any successful cloak must preserve straight axial columns rather than rerouting topology. Screening nine equal-mass insert architectures on an Euler–Bernoulli frame surrogate under a shared optimization budget confirms that altering connectivity is counterproductive (Supplementary Fig. S1a). Requiring any geometric modification to improve frame-model J by at least 0.10 beyond baseline pure width grading (0.484) disqualifies relaxing the upper width bound to 4mm (0.442) and permitting member deletion (0.471), both of which violate fabrication rules for negligible gain. Adding radial braces (0.509) or halving joint bending stiffness (0.510) gives no advantage, while X-bracing (0.845) and hoop bracing (0.862) degrade cloaking by locking up annular shear. Coordinate-warped direct lattice transformation (DLT [17, 18]) with uniform strut widths curves axial columns into compliant bending arcs and amplifies mismatch to $J = 1.87–3.02$—far worse than the bare hole. Rebuilding the best graded-pitch candidates on the high-fidelity continuum pipeline confirms that pure width

grading (Graded cloak, $J = 0.559$; Warm-start, 0.575) outperforms both *xy*-graded pitch ($J = 0.591$) and radially graded pitch (0.594; Table 1, Supplementary Fig. S1b and Supplementary Table S3).

Holding nodal coordinates fixed within the annular cloak ($r_{\mathrm{void}} = 30\mathrm{mm}$, $r_{\mathrm{cloak}} = 55\mathrm{mm}$; Fig. 2a), we optimize 500 mid-span widths b_m and 484 tapered joint-neck widths b_e subject to exact solid-area neutrality ($A(\boldsymbol{x}) = A_{\mathrm{REF}}$, matching intact $A_{\mathrm{REF}} = \overline{\rho} L^2 = 7875\mathrm{mm}^2$ to within 0.01% at converged Boolean area 7,874.6 mm^2) and SLS polymer printability limits ($0.5\mathrm{mm} \le b_m, b_e \le 2.0\mathrm{mm}$, minimum clear gap $\ge 0.5\mathrm{mm}$; Methods [26, 40]). Tapering joint necks below mid-span widths selectively lowers local bending stiffness (which scales as b^3) while keeping axial column stiffness high (scaling linearly with b), decoupling diagonal shear compliance from orthogonal load carrying. Starting from uniform $b_{\mathrm{ref}} = 0.938\mathrm{mm}$, multi-fidelity trust-region optimization over the four axial platen loads $\mathcal{L}_0$ cuts worst-case rigid-body-removed displacement mismatch by 44% ($J = 0.559$, $J_{\mathrm{raw}} = 0.546$, reaction ratio $J_R = 0.855$, far-field ratio $J_{\mathrm{far}} = 0.441$; Table 1). Initializing from a prior displacement-loaded design (Warm-start) reaches a slightly higher local minimum ($J = 0.575$, $J_{\mathrm{raw}} = 0.565$), while sibling runs agree within 0.0003 across all mesh refinements (Supplementary Table S1a). Spatially, the Graded cloak self-organizes into a near-binary architecture: 2.0 mm column and row bundles flank the hole to carry bypassed axial force, while diagonal quadrants pair widened mid-spans with slender 0.50 mm compliant joint necks (Fig. 2b, c). Under frictionless *y*-compression, short transverse struts act as lintels that divert interrupted column loads laterally into reinforced side bundles carrying 1.5–2 times the far-field intact force while restoring outer columns toward unity (Fig. 2d).

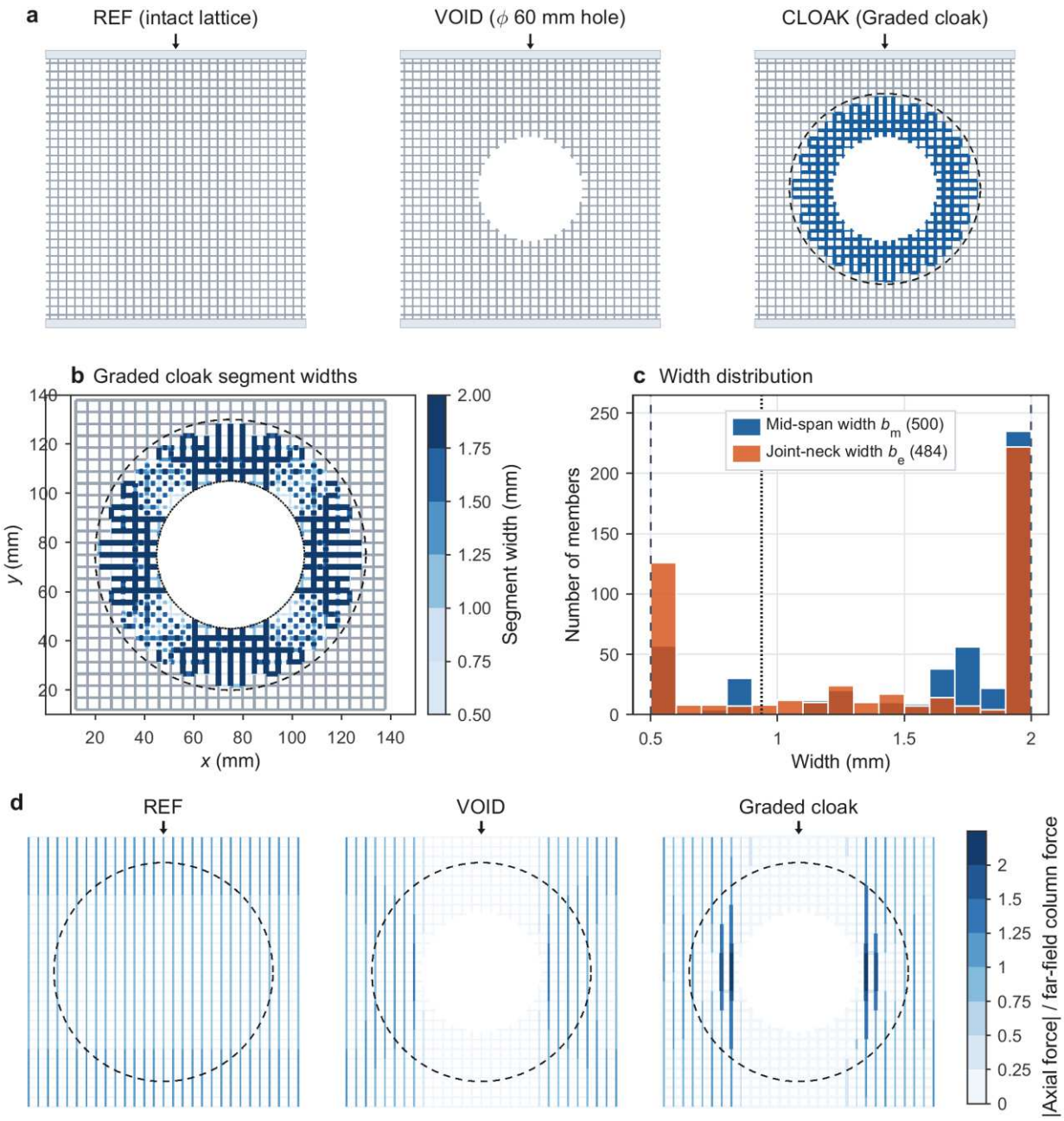

Fig. 2 | Mass-neutral width-graded cloak geometry and lateral load bypass in a square lattice. a, Intact reference (REF, cell pitch 4.84mm, $\overline{\rho} = 0.35$), unreinforced void (VOID, diameter 60mm), and mass-neutral Graded cloak inside the $150\text{mm} \times 150\text{mm}$ plate with 5mm loading platens (dashed circle marks $r_{\text{cloak}} = 55\text{mm}$). **b**, Spatial distribution of optimized segment widths inside the annulus (gray: unmodified background at $b_{\text{ref}} = 0.938\text{mm}$). **c**, Histograms of mid-span widths b_m (500 members) and joint-neck widths b_e (484 tapered struts); dashed lines denote $b_{\min} = 0.5\text{mm}$ and $b_{\max} = 2.0\text{mm}$, and the dotted line marks b_{ref}. **d**, Normalized axial member force under frictionless *y*-compression in the beam model, illustrating lateral load diversion around the opening.

Full-field continuum displacement maps $|\boldsymbol{u} - \boldsymbol{u}_{\text{REF}}|$ outside $r = 55.5$ mm show that the Graded cloak strongly attenuates the platen-spanning error streaks generated by VOID under both frictionless *y*- and *x*-compression (Fig. 3, inset ratio 0.55 rounding $h = 0.1$ mm raw ratio 0.549). Radial error-energy partitioning demonstrates that 45% of residual error energy sits inside a single-cell transition collar $r \in [55.5,60]\text{mm}$ (local CLOAK/VOID ratio 0.66), falling sharply to 0.49 in the $60-70\text{mm}$ band and 0.45 across $70-90\text{mm}$, with less than 3% beyond

90mm (Supplementary Fig. S2). Examining pixelwise Q6 von Mises stress within 69 mm of the plate center (excluding end bars) shows that the worst 99th-percentile stress ratio improves slightly from 1.28 (VOID) to 1.24 (cloak; 1.28 vs. 1.23 in *y*-compression), whereas the 99.9th-percentile peak rises from 1.24 to 1.44 at the narrowed 0.50 mm necks. Scaling linear nominal strain (for example to 0.25%, well below the 0.72% pinned-end out-of-plane critical buckling strain and 29–48% in-plane bifurcation limits; Supplementary Note 1) reduces local stresses proportionally relative to polymer yield (Supplementary Note 2).

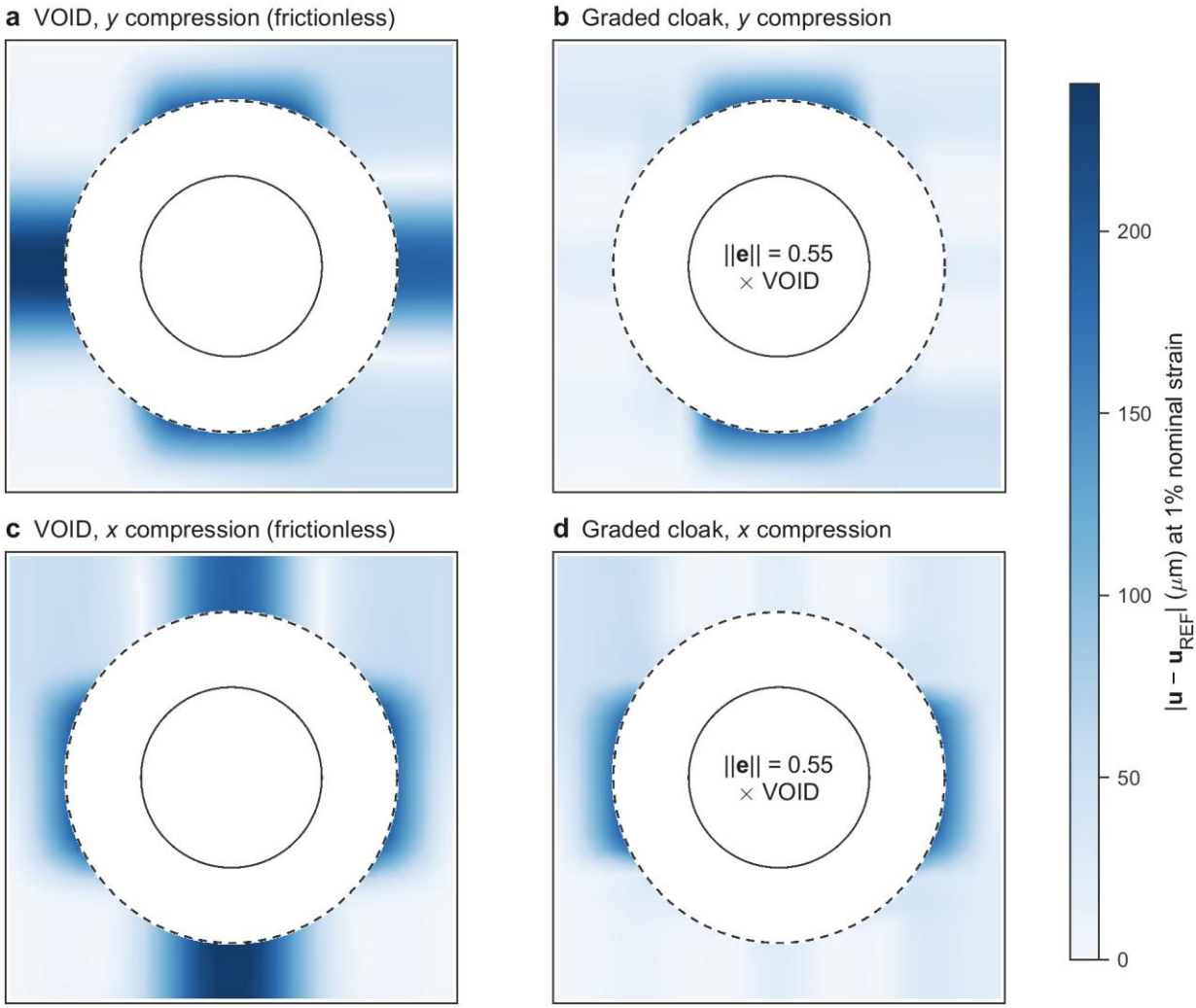

Fig. 3 | Exterior displacement invisibility under uniaxial platen compression. Exterior displacement mismatch $|\boldsymbol{u} - \boldsymbol{u}_{\mathrm{REF}}|$ outside $r = 55.5\mathrm{mm}$ evaluated on the continuum mesh ($h = 0.1\mathrm{mm}$, 1% nominal strain; shared color scale capped at the 99th percentile of VOID, $240\mu\mathrm{m}$). **a, b**, Frictionless *y*-compression for VOID (**a**) and Graded cloak (**b**). **c, d**, Frictionless *x*-compression for VOID (**c**) and Graded cloak (**d**). Inset annotations report the rounded continuum norm ratio (0.55 vs. 0.549 unrounded at $h = 0.1$ mm).

Manufacturing-tolerance robustness is verified via paired Monte Carlo simulations perturbing strut widths across REF, VOID, and CLOAK identically with spatially correlated scatter $\delta b(\boldsymbol{x}_e) = \sigma_b f(\boldsymbol{x}_e)$ (20 mm correlation length, 400 Fourier modes; Supplementary Note 2, Supplementary Table S5 and Supplementary Fig. S4) [40, 41]. At $\sigma_b = 0.06\mathrm{mm}$, every virtual print of the Graded cloak outperforms its paired VOID plate over the full domain Γ (median/max $J = 0.615 / 0.812$), optical marker subsets ($0.667/0.862$), and far field ($0.553/0.909$). Across 40 extended realizations, rigid-body-removed marker displacements surpass VOID up to $\sigma_b = 0.08\mathrm{mm}$ ($P_{95} = 0.89$),

whereas unprojected J_{raw} remains below unity up to $\sigma_b \approx 0.044\mathrm{mm}$ because geometric noise chiefly introduces harmless rigid-body platen drift.

Evaluating the fixed platen-trained cloak under held-out boundary fields following Senhora et al. [27] spans three complementary test tiers (Fig. 4 and Supplementary Table S10). First, on the continuum model, the Graded cloak improves upon VOID across all eight held-out named loads—traction-free *y*- and *x*-uniaxial compression (ratio 0.61), equal biaxial compression (0.94), clamped shear (0.53), axial strain gradient (0.83), and the three dominant fourth-order VOID boundary-displacement eigenmodes (0.81–0.97)—spanning 6.1–19.7% bare-hole error and beating Warm-start on every case (Fig. 4a). Second, across 2,000 random fourth-order boundary fields, it achieves 100% success (45/45) in the beam model and 98% (108/110) in continuum Q6 whenever VOID error reaches at least 10%, while averaging 48% across all 2,000 draws because shear-rich fields leave the bare hole barely visible (Fig. 4b, c; worst hole-sensitive subspace ratio 1.24 in continuum vs. 0.987 in beam). Third, across uniform in-plane strain orientations, the cloak beats VOID over 93% of directions (mean 0.957), amplifying error only near pure shear (2.67% vs. 0.77% in VOID) because thickened orthogonal bundles inadvertently raise the ring shear modulus by $m \approx 3\times$.

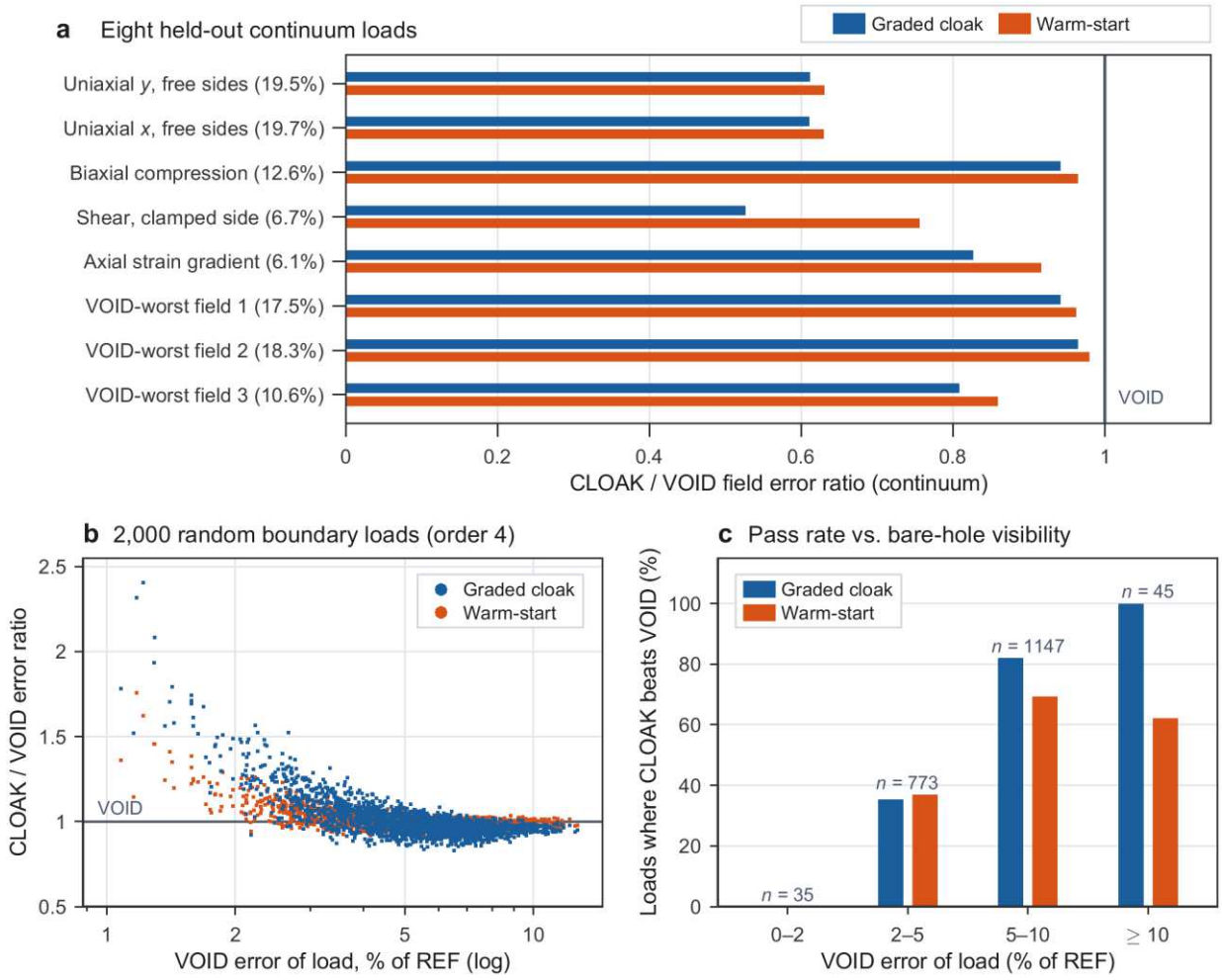

Fig. 4 | Generalization of the platen-trained cloak to unseen boundary loads. a, Continuum error ratios relative to VOID across eight held-out load cases (labels indicate bare-hole mismatch vs. REF): the Graded cloak improves upon both VOID and the Warm-start design in every case. **b**, Ratio across 2,000 random fourth-order polynomial boundary displacement fields vs. bare-hole visibility (frame model). **c**, Stratified pass rate confirming near-universal improvement once bare-hole visibility reaches ≥10% (full continuum audit in Supplementary Table S10).

Classical shear-lag mechanics [42] explains both why lateral load transfer requires wide lintels and why spatial width grading outperforms homogeneous rings. Balancing axial column stiffness $EA = E_s b_c t$ against transverse row bending stiffness $k_s = 12E_s I/\ell^3$ yields $EA\, v_{yy} + k_s \ell\, v_{xx} = 0$, defining a characteristic lateral load-transfer length

$$\Lambda = \ell \sqrt{\frac{b_c\, \ell^2}{b_r^3}} \tag{3}$$

At uniform reference width $b_{\mathrm{ref}} = 0.94\mathrm{mm}$, $\Lambda = 25\mathrm{mm} \approx 5.2\,\ell$ spans the entire cloak annulus, whereas thickening both columns and lintels to $b_{\mathrm{c}} = b_{\mathrm{r}} = b_{\max} = 2.0\mathrm{mm}$ compresses transfer to $\Lambda_{\min} = 11.7\mathrm{mm} \approx 2.4\,\ell$, completing diversion inside Ω_c. Conversely, an exhaustive parametric search across all uniform D_4-symmetric continuum rings ($(C_{11}^r, C_{12}^r, C_{66}^r)$ over r = 30–55 mm) subject to equal mass ($C_{11}^r \le 1.42\, C_{11}$), non-auxetic bounds ($\nu \ge 0$), and shear neutrality reaches only $J = 0.88$ at $\lambda = 3$ and $J = 0.96$ at $\lambda = 80$ (Supplementary Fig. S3a); allowing 3× stiffening and auxetic Poisson ratios still restricts shear-neutral homogeneous rings to $J = 0.73$ at $\lambda = 80$. Across all uniform strains (Supplementary Fig. S3b), optimal uniform rings approach bare-hole parity (0.997), while thin polar-orthotropic neutral shells [6] degrade from $0.82-0.97$ in isotropic sheets to $2.1-2.2$ at $\lambda = 65$ because polar anisotropy mismatches Cartesian lattice axes. Spatial width grading overcomes this constitutive barrier by separating stiff orthogonal load highways from compliant diagonal shear hinges.

Evaluating sensitivity to two-dimensional plate idealizations confirms that the underlying load-bypass physics holds across thickness regimes (Supplementary Note 1 and Supplementary Table S2). On three-dimensional hexahedral unit cells at reference strut width 0.94 mm, effective axial modulus exceeds plane stress by 3.5% and shear modulus rises by 13%, reducing the effective stiffness ratio by ~8%; at the full plate scale, replacing plane stress with plane strain shifts the raw platen ratio of the Graded cloak modestly from 0.546 to 0.599 while leaving its reaction ratio invariant at 0.855 and pure-shear ratio unchanged at 3.45.

Table 1 | Summary of mass-neutral lattice cloak performance across architectures, topologies, and debiasing regimes.

Series & design	Anisotropy λ	Platen J_{raw} / J	Reaction J_R	Pure shear r_V (r_s)	Order-4 pass % (VOID ≥ 10%)
Square ($\bar{\rho}$ = 0.35, 30/55 mm)					
Graded cloak ($\mathfrak{L}_0$ only)	65 (45.7*)	0.546 / 0.559	0.855	3.45 (3.45)	48% (98%)
Warm-start cloak ($\mathfrak{L}_0$ only)	65 (45.7*)	0.565 / 0.575	0.888	—	—
Epigraph shear-controlled (s = 1.5)	65 (45.7*)	0.664 / 0.677	0.929	1.03	99% (100%)
Soft-mode debiased ($r_s \le 1.02$)	45.7*	0.597 / 0.605	—	— (1.02)	98.5%
Five-topology comparison ($\mathfrak{L}_0$ only)					
Square ($\bar{\rho}$ = 0.30)	81	0.525 / 0.533	0.859	5.01	48% (100%)
Honeycomb ($\bar{\rho}$ = 0.35)	10 ($\bar{\rho}$=0.30)	0.624 / 0.697	0.898	1.06	88% (99%)
Triangular ($\bar{\rho}$ = 0.30)	3.2	0.569 / 0.630	0.631	0.93	99% (100%)
Braced square ($\bar{\rho}$ = 0.3145)	4.2 ($\bar{\rho}$=0.30)	0.543 / 0.584	0.491	0.85	99% (100%)
Density & orientation debiasing					
Square (0°, $\bar{\rho}$ = 0.25): Uncon. / Deb.	99.7*	0.525 / 0.563	—	— (6.08 / 0.99)	60.4% / 5.2%
Square (45°, $\bar{\rho}$ = 0.35): Uncon. / Deb.	44.4*	0.381 / 0.606	—	— (3.20 / 1.00)	93.7% / 100.0%
Archimedean 4.8.8 (0°, $\bar{\rho}$ = 0.30, $\mathfrak{L}_0$)	16.9*	0.324 (0.1 mm)	—	— (0.64; 0.619 free)	87.0%

Platen metrics evaluated on continuum Q6 at h = 0.05 mm (except 4.8.8 at h = 0.10 mm); unseen order-4 evaluations at h = 0.10 mm. Asterisks denote measured principal-frame continuum ratios λ_{pr}. For Density & orientation debiasing rows,

column 3 lists unconstrained vs. debiased J_{raw}. Complete datasets appear in Supplementary Tables S3, S8, S9, S13, S14 and S16.

Equal-mass packing threshold and zero-optimization scale transfer

For practical engineering integration around variable cutout sizes, conserving intact solid area $\overline{\rho}$ inside an annular cloak whose maximum packable solid fraction is $\rho_{\max}$ imposes an unavoidable geometric lower bound on outer cloak radius:

$$\overline{\rho}\,\pi r_{\text{cloak}}^2 \le \rho_{\max}\,\pi(r_{\text{cloak}}^2 - r_{\text{void}}^2) \implies \frac{r_{\text{cloak}}}{r_{\text{void}}} \ge \left(1 - \frac{\overline{\rho}}{\rho_{\max}}\right)^{-1/2} \tag{4}$$

At $\overline{\rho} = 0.35$ and $b_{\max} = 2.0\text{mm}$, rasterized orthogonal intersections achieve $\rho_{\max} = 0.56\text{–}0.60$, yielding minimum feasible radius ratios of 1.64, 1.59, and 1.56 (summarized as $r_{\text{cloak}} \gtrsim 1.6\, r_{\text{void}}$) for opening radii $r_{\text{void}} = 20{,}30{,}$and 40 mm, respectively (Fig. 5a). Rings narrower than this geometric bound can accommodate only 88–98% of the removed solid mass, saturate solidly against the width cap into stiff collars, and markedly worsen hole visibility ($J = 0.97\text{–}1.54$).

Across six feasible square-lattice geometries spanning $r_{\text{void}} \in \{20{,}30\}\text{mm}$ and insert widths $w = r_{\text{cloak}} - r_{\text{void}} \in [3.5{,}6.6]\,\ell$ (Fig. 5a and Supplementary Table S7), re-optimized continuum platen ratios obey an empirical saturating scaling law governed directly by the minimal shear-lag transfer length $\Lambda_{\min} = 2.4\,\ell$:

$$J_{\text{re-opt}} \approx 0.777 - 0.073\,\frac{r_{\text{void}}}{\ell} + 0.428\exp\left(-\frac{w - w_{\min}(r_{\text{void}})}{\Lambda_{\min}}\right) \tag{5}$$

Equation (5) reproduces both narrow-margin crowding (0.690 at 30/50 mm) and wide-ring saturation with RMSE = 0.011 (leave-one-out RMSE = 0.023, halving the 0.046 error of a linear baseline). Leveraging square-lattice D_4 symmetry, folding the 30/55 mm Graded cloak into a single octant of six radial bins, three 15° angular bins, and column versus row orientation condenses the full spatial pattern into a compact 36-entry lookup table of median b_m and b_e widths (Fig. 5b, c). Across all five geometries whose annulus width exceeds the equal-mass packing bound by at least 0.85 cell pitches, direct table lookup without optimization achieves raw platen ratios of 0.566–0.873—recovering 54–82% of full re-optimized gain (82% on the source geometry and 54–78% across unseen receiving geometries; Supplementary Table S7). Only at the minimal margin of 0.47 cell pitches (30/50 mm) does direct lookup break down (1.169 vs. 0.690 after optimization).

Scanning the empirical constraint–performance frontier of graded D_4 continuum rings at 30/55 mm ($\lambda = 65$; Supplementary Fig. S5) shows that tripling the stiffness contrast cap ($2.13 \to 6\text{mm}$) or adding 50% extra mass lowers J only modestly from 0.550 to 0.475–0.509. Platen contact-pressure profiles explain this plateau (Supplementary Table S4): extreme square anisotropy casts a deep Saint-Venant column shadow ($\sim D\sqrt{\lambda}/\pi \approx 130\text{mm}$ [43, 44]) where platen traction behind the hole remains near zero (profile L_2 error improving only 0.58→0.54; CoV 0.75→0.69 vs. REF 0.004), whereas low-λ triangular and braced-square backgrounds retain 18–25% contact traction behind VOID (rising to 37% with cloaking) and cut profile error by 30–37%. Finally, evaluating wide rings on fixed common outer probes ($r \ge 65.5\text{mm}$; Supplementary Note 5 and Supplementary Table S17) shows that widening the annulus from 5.2 to 7.2 cells lowers the conservative epigraph shear-neutrality penalty from 1.87 to 1.34 (and to 1.14 for a 20/55 mm cutout), whereas platen-only training overfits to $\mathcal{L}_0$ and amplifies pure-shear error up to 4.58–5.81× VOID.

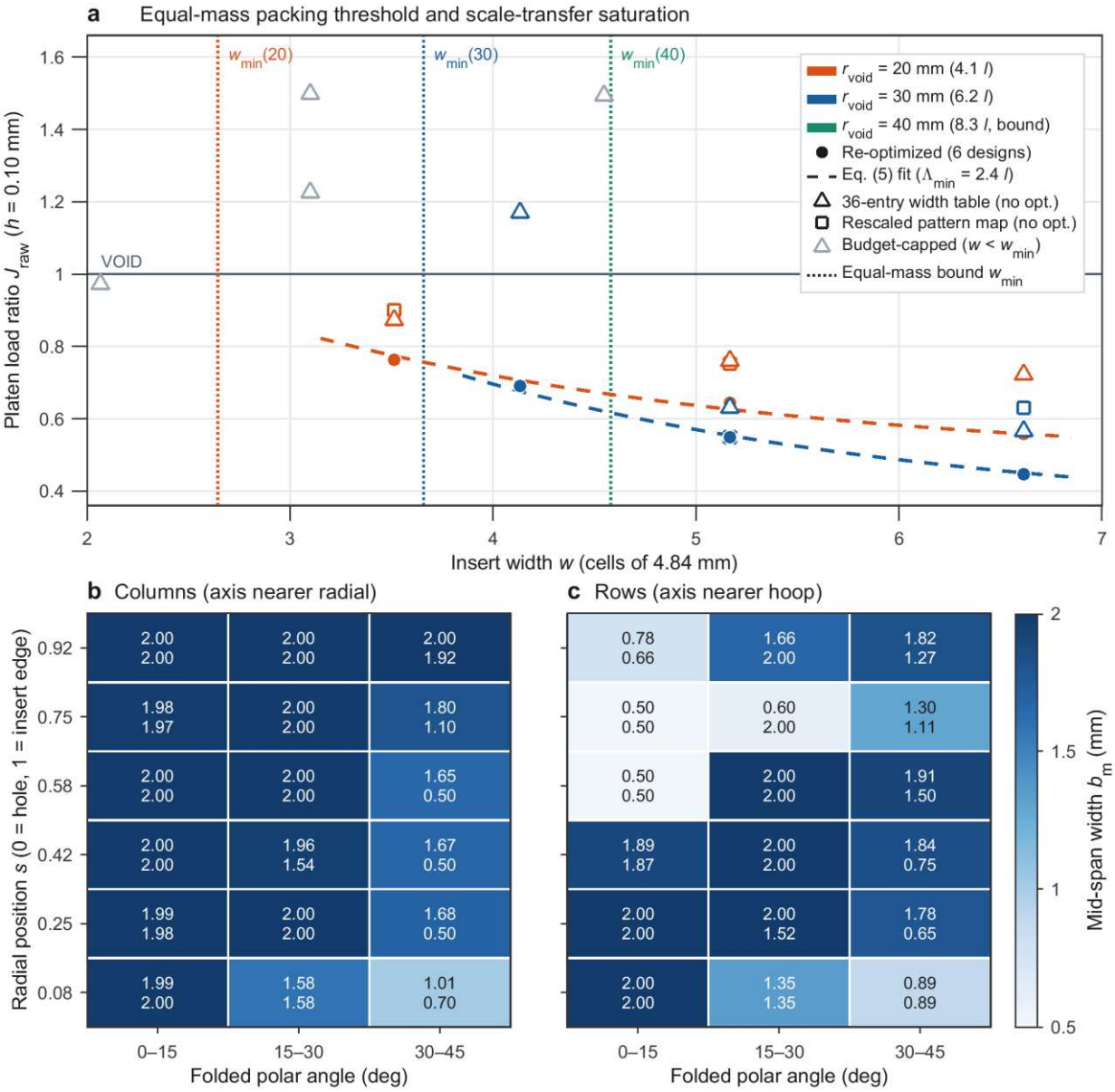

Fig. 5 | Equal-mass packing threshold, shear-lag saturation, and zero-optimization scale transfer. a, Converged raw platen ratio J_{raw} vs. annulus width w in cell pitches ($h = 0.1$mm). Dashed curves show Equation (5) ($\Lambda_{\mathrm{min}} = 2.4\,\ell$) with RMSE = 0.011; vertical dotted lines mark equal-mass packing limits w_{min} (infeasible rings shown in gray). Open triangles and squares compare zero-optimization transfer via the 36-entry width table and coordinate rescaling against full re-optimization (filled circles; tabulated in Supplementary Table S7). **b, c**, Condensed 36-entry width lookup table (mm) extracted from the 30/55 mm Graded cloak for predominantly radial columns (**b**) and predominantly hoop rows (**c**), reporting median mid-span width b_m (upper entry) and joint-neck width b_e (lower entry).

Lattice topology and fiber-limit theory of soft-mode bias

Applying the identical equal-mass pipeline across five background lattices reveals how topology governs multi-load generalization (Table 1, Supplementary Fig. S6 and Supplementary Table S8; geometric adjustments documented in Supplementary Note 3). Reducing background anisotropy to $\lambda = 3.2$ (triangular) or $\lambda = 4.2$ (diagonal-braced square) yields natural shear neutrality under platen-only training: both achieve 100% pass rates across uniform strain orientations (worst ratios 0.93 and 0.85), braced square delivers the lowest platen reaction mismatch ($J_R = 0.491$) even with 69% of struts at b_{min} via direct diagonal load paths, and uniform thickening alone achieves 0.90–0.99 (versus ~1.5 in plain square). Nevertheless, four of the five platen-trained designs retain

isolated fourth-order hole-sensitive eigenmodes above unity (1.20–1.91); augmenting training with the six worst VOID eigenmodes boosts triangular and honeycomb random pass rates (99%→100% and 88%→97%) at the cost of platen fidelity (0.57→0.81 and 0.62→0.87; Supplementary Table S11). Rotating the $\overline{\rho} = 0.35$ square lattice by $\theta \in [5^{\circ}, 45^{\circ}]$ proves that directional bias tracks the background's softest Kelvin eigen-strain $\boldsymbol{\varepsilon}_s$ [45] rather than loading axes: at symmetric angles $\theta = 0^{\circ}, 45^{\circ}$ (zero shear–extension coupling $\eta_{16} = 0$), tiny bare-hole soft-mode visibility (0.77– 0.86%) drives severe amplification ($r_s = 3.45$ and 3.20 at $\overline{\rho} = 0.35$; 6.08 and 5.67 at $\overline{\rho} = 0.25$), whereas coupled intermediate angles ($\theta = 5^{\circ}$– 22.5°, η_{16} = 0.47–0.59) activate platen interactions that attenuate bias to 1.34– 1.88.

An asymptotic fiber-limit theory accounts quantitatively for both bare-hole scaling and bias onset whenever shear-lag transfer exceeds plate half-width, $a\sqrt{\lambda} > H$ ($\lambda > (H/a)^2 \approx 6$ for $H = 75\text{mm}, a = 30\text{mm}$). Severed axial fibers move nearly rigidly with platens, yielding geometric axial visibility $K_{\varepsilon} = 11.56\%$ (11.7–11.8% in discrete lattices, 11.0% in continua), while tangent fibers balancing lost shear traction $\tau_0 = C_{66}\gamma$ develop an edge-singular strain profile:

$$\varepsilon_f(y) = -\frac{\gamma}{\lambda}\frac{y}{\sqrt{a^2 - y^2}}, \quad \Delta_{\gamma} = \frac{K_{\gamma}}{\lambda} \tag{6}$$

Integrating this singularity produces a gentle logarithmic width sensitivity (pre-factor 2.98 at 0.5 mm vs. 2.53 at 1.0 mm, matching 3.4 across 19 lattices). At the cloak outer edge, any uncompensated ring shear stiffening $k > 1$ generates an interface traction jump $(k-1)\tau_0$ responsible for ~90% of soft-mode bias (Supplementary Fig. S8b), reaching the asymptotic ceiling at $H/a = 2.5$:

$$r_{\infty}(k) \approx \sqrt{k^2 - 0.4\,k(k-1) + 19.4\,(k-1)^2} \tag{7}$$

in close agreement with continuum asymptotes (4.7,9.2,18 vs. 4.9,9.5,17.5 for $k = 2,3,5$). Finite plate geometry collapses normalized axial visibility (Fig. 6a) and bias onset across $H/a \in \{2.5, 3.5, 5\}$ onto one dimensionless parameter:

$$\xi = \frac{a\sqrt{\lambda}}{H} \tag{8}$$

following the master crossover $(r-1)/(r_{\infty}(k)-1) \approx 1 - 1.25/\xi$ within 5% for $\xi \geq 1.5$ and suppressing bias below $\xi \approx 1.2$ (Fig. 6b). Notably, the apparent growth of r_s across decreasing densities (1.46% → 0.33%) stems from the vanishing VOID denominator (3.85% → 2.03%), even though absolute cloak soft-mode error decreases (3.85%→2.03%). Meanwhile, the effective ring stiffness–width exponent $m_{\text{eff}} = 1 + m_{\text{soft}} - m_{\text{stiff}}$ separates low-bias stretching rings ($m = 1$, 1.08–1.82) from high-bias bending rings ($m = 3$, up to 5.60; Fig. 6c).

Querying a precomputed continuum ring table $r(\lambda_{\text{pr}}, m_{\text{eff}})$ using intact elastic parameters alone predicts measured platen-trained bias within 1.3 × (1/1.3 to 1.3; log-rms error 0.13) across seven of eight tested topologies—spanning Square, Laguerre L1–L3, and unseen Honeycomb, Braced square, and Triangular lattices (Fig. 6d, Supplementary Figs. S9–S10 and Supplementary Tables S12, S18). The sole counterexample is the Archimedean 4.8.8 lattice [36], whose high Poisson ratio ($C_{12}/C_{11} = 0.87$) defines a deviatoric soft mode $d_{\text{s}} = (0.707, -0.707, 0)$. Because bare-hole visibility along this mode is already 4.05% (fivefold larger than in square plates), four-load training yields $r_{\text{s}} = 0.639$ instead of the predicted 1.63. Controlled subset ablation with identical initialization and budget confirms that mixed clamping is unnecessary: frictionless uniaxial compression alone reaches $r_{\text{s}} = 0.619$, beating both all four platen loads (0.639) and bonded platens alone (0.682; Fig. 6e and Supplementary Table S16) because uniaxial elongation already projects strongly onto the deviatoric mode.

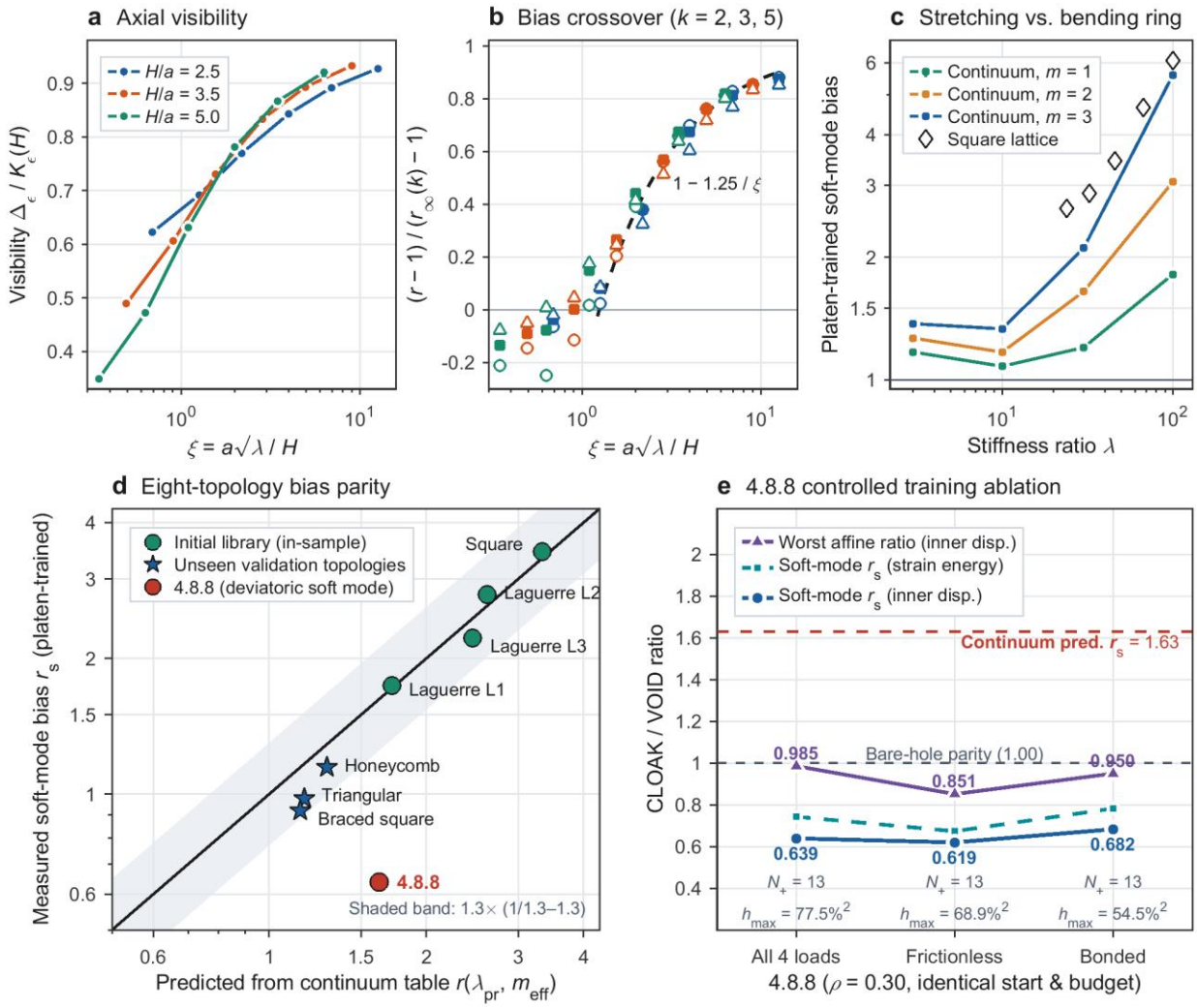

Fig. 6 | Fiber-limit soft-mode bias theory and the Archimedean 4.8.8 counterexample. a, Collapse of normalized axial bare-hole visibility onto dimensionless scale parameter $\xi = a\sqrt{\lambda}/H$ across aspect ratios $H/a \in \{2.5,3.5,5\}$. **b**, Universal crossover of bias amplitude $(r-1)/(r_\infty(k)-1) \approx 1 - 1.25/\xi$ across aspect ratios and outer shear factors $k \in \{2,3,5\}$. **c**, Separation of stretching-dominated (m = 1) vs. bending-dominated (m = 3) optimal continuum rings compared with square lattices. **d**, Parity between measured soft-mode bias and precomputed continuum prediction $r(\lambda_{\mathrm{pr}}, m_{\mathrm{eff}})$ across eight topologies (shaded band: 1.3 × spanning 1/1.3–1.3; geometries in Supplementary Fig. S10 and constants in Supplementary Tables S12, S18). **e**, Controlled training-subset ablation on the high-Poisson 4.8.8 lattice ($\bar{\rho} = 0.30$): frictionless uniaxial compression alone suffices to suppress soft-mode bias ($r_s = 0.619$).

Debiasing cost and full-space 25-dimensional operator error redistribution

Evaluating the cost of restoring multi-load neutrality in square lattices, we test both minimax epigraph shear control $\mathrm{minmax}(J, r_\gamma/s)$ ($s \in \{2,1.5,1\}$; Supplementary Fig. S7 and Supplementary Table S9) and bounded-tolerance continuation $r_s \leq 1.02$ across relative density and lattice orientation (Fig. 7a, b and Supplementary Table S13). At relative density 0.35, setting s = 2 cuts the pure-shear ratio from 3.45 to 1.21 for a minor raw platen cost of 0.051 (rising from 0.546 to 0.597); tightening to s = 1.5 reduces pure-shear ratio to 1.03 (raw J = 0.664, RBM-free 0.677), pushes order-4 random pass rates from 46% to 99%, reduces worst hole-sensitive subspace error to 0.992, and bounds sixth-order worst ratios to 1.05–1.25 (versus 4.29 unconstrained). Note that in the unpaired Monte Carlo sampling of Supplementary Table S9 vs. Table S8, random-load pass rates differ slightly (46% vs. 48%) while the deterministic truncated subspace peak (1.216 vs. 1.24) reflects fixed audit discretization. By contrast, forcing braced-square shear ratios below 0.7 similarly incurs heavy platen penalties

(0.89–1.16). Across converged continuation runs with $\theta \leq 22.5^{\circ}$ and $\overline{\rho} \leq 0.40$, imposing $r_s \leq 1.02$ incurs a manageable 4–18% raw platen penalty—stabilizing cleanly under mesh refinement from +25.50% at 0.10 mm to +17.72% at 0.05 mm and +17.03% at 0.0375 mm for θ = 0°, $\overline{\rho} \leq 0.40$ (Supplementary Table S1b). At 45°, however, debiasing increases raw mismatch by +59% at $\overline{\rho} = 0.35$ (0.381→0.606) and +75% at $\overline{\rho} = 0.25$ (0.430→0.753), eliminating the apparent 45° platen advantage (Fig. 7b). At relative density 0.45, continuation fails to drop below r_s = 1.46 because stocky nodal junctions invalidate slender-beam adjoints [39].

Auditing the entire 25-dimensional fourth-order polynomial boundary-displacement space without subspace truncation tests negative-semidefiniteness $\boldsymbol{Q}_W \preceq \mathbf{0}$ via the generalized eigenvalue problem

$$\boldsymbol{Q}_W = \boldsymbol{E}_C^{\mathrm{T}} \boldsymbol{W} \boldsymbol{E}_C - \boldsymbol{E}_V^{\mathrm{T}} \boldsymbol{W} \boldsymbol{E}_V, \quad \boldsymbol{Q}_W \boldsymbol{q} = \eta \, \boldsymbol{G}_R \, \boldsymbol{q} \tag{9}$$

where $\boldsymbol{G}_R$ is the protocol-matched intact reference Gram matrix and $h_{\max} = 10^4 \eta_{\max}(\boldsymbol{Q}_W, \boldsymbol{G}_R)$ measures incremental peak error in $\%^2$ (Methods). Five nested protocols isolating rigid-body projection, cutoff radius ($r \geq$ 55.5 vs. 58.0 mm), and displacement versus Q6 strain-energy norms (Fig. 7c, d and Supplementary Note 4, Tables S14–S16) uncover three structural behaviors. First, positive excess modes persist across all 11 designs (3 to 13 positive eigenvalues above counting tolerance), showing that favorable truncated-subspace metrics coexist with residual amplification in general non-affine loads. Second, at low density ($\overline{\rho} = 0.25$, $\theta = 0^{\circ}$), enforcing soft-mode control lowers raw peak displacement excess from +24.90 to +13.59 $\%^2$ (+22.82 to +13.58 $\%^2$ RBM-free), yet collapses the dominant negative eigenvalue magnitude from −38.03 to −1.97 $\%^2$ (−39.12 to −2.01 $\%^2$ RBM-free) while six positive modes remain, collapsing the 2,000-load random pass fraction from 60.4% to 5.2% (65.1% to 5.3% RBM-free; Fig. 7c). Third, evaluating the exact same outer pixels ($r \geq 58.0$mm) under displacement L_2 error leaves results insensitive to projection or cutoff shift ($+1.47\ \%^2$ inner raw → $+1.48\ \%^2$ inner RBM-free → $+0.96\ \%^2$ outer RBM-free; pass rate 98.5% → 98.2% → 97.5%), whereas switching to normalized Q6 strain energy updates both $\boldsymbol{Q}_W$ and $\boldsymbol{G}_R$, amplifying peak excess to $h_{\max} = +178.8\ \%^2$ and shifting r_s from 1.021 to 1.150 due to sharp local strain gradients inside the boundary collar (Fig. 7d). In ultra-anisotropic regimes ($\lambda \approx$ 99.7), intermediate epigraph weights (s = 1.5–2) therefore preserve broad axial gains far more effectively than strict unbiasedness.

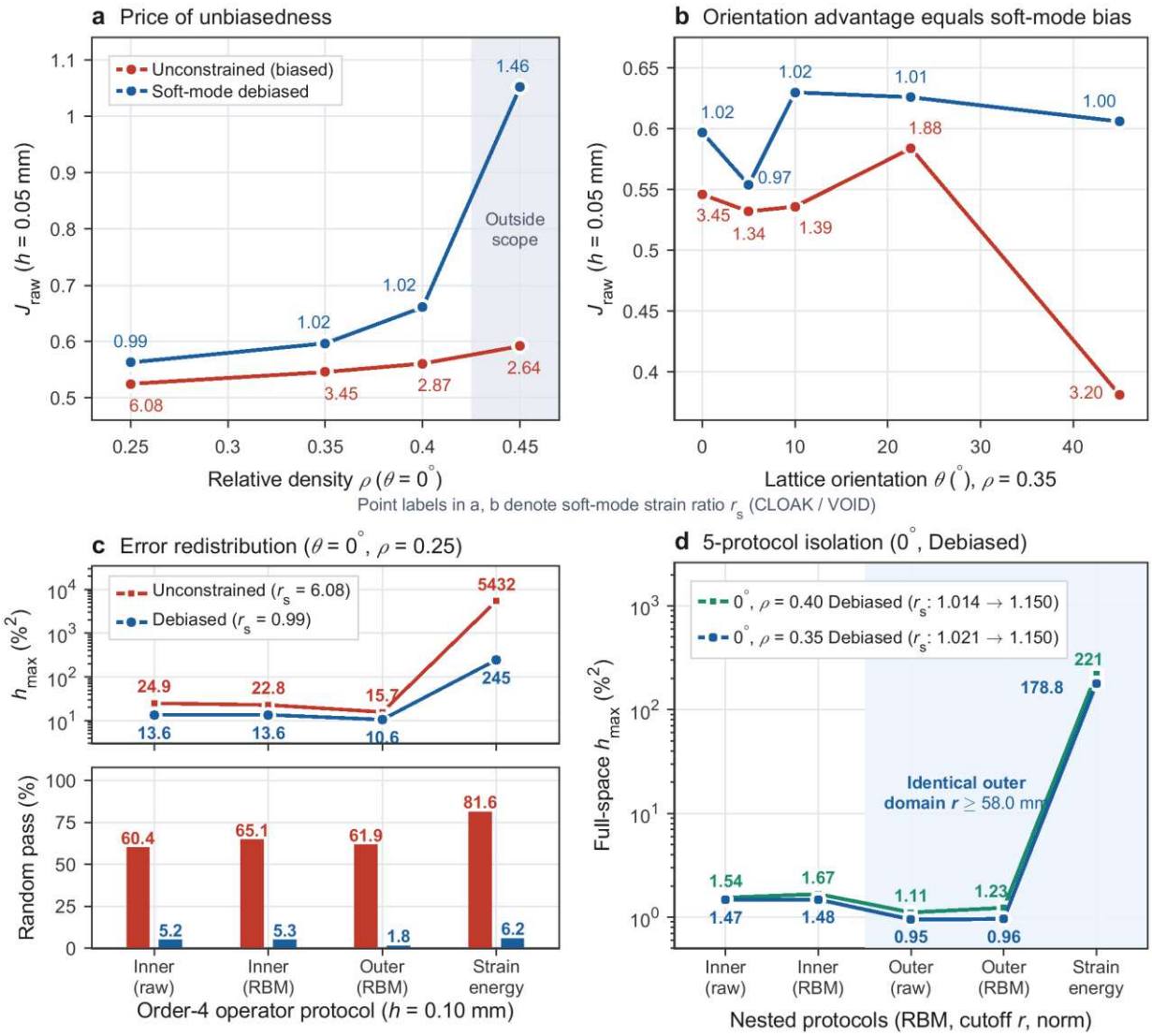

Fig. 7 | Cost of debiasing and full-space 25-dimensional operator error redistribution. a, Raw platen penalty of enforcing $r_s \leq 1.02$ across relative density at $\theta = 0^\circ$ (shaded $\overline{\rho} = 0.45$ exceeds thin-strut beam surrogate scope; labels show soft-mode ratio r_s). **b**, Collapse of the apparent 45° platen advantage at $\overline{\rho} = 0.35$ onto 0° parity once soft-mode bias is controlled. **c**, Spectral error redistribution at $\overline{\rho} = 0.25$, $\theta = 0^\circ$: debiasing lowers peak excess $h_{\max} = 10^4 \eta_{\max}(\boldsymbol{Q}_W, \boldsymbol{G}_R)$ (top) while reducing the 2,000-load random pass rate from 60.4% to 5.2% (bottom). **d**, Nested five-protocol isolation at $\overline{\rho} = 0.35$ and 0.40 showing minimal shift from rigid-body projection or inner/outer cutoff vs. two-order-of-magnitude amplification under normalized Q6 strain energy on identical $r \geq 58.0\text{mm}$ pixels (complete 11-design and 5-protocol spectra in Supplementary Tables S14–S16).

Discussion

Evaluated strictly against the unbiased multi-load standard of Senhora et al. [27], width-graded cloaking in high-anisotropy lattices is neither an ideal omnidirectional transformation cloak nor a fragile single-load patch. Because bare-hole visibility across 19 homogenizable lattices obeys the universal inverse law $\Delta_\gamma/\Delta_\varepsilon \approx 3.4/\lambda$ ($r^2 = 0.97$, Fig. 1), keeping straight load-bearing square-lattice columns unbroken while placing 0.50 mm compliant joint necks in diagonal quadrants yields a 44% worst-case platen improvement ($J = 0.559$) that generalizes across all eight held-out continuum loads, 98% of strongly visible random fourth-order fields, and all paired stochastic width-scatter realizations up to $\sigma_b = 0.06$ mm, degrading selectively only near pure shear (2.67% vs. 0.77% in

VOID; Figs. 2–4). Exhaustive D_4 continuum ring optimizations prove that spatial width grading breaks equal-mass and non-auxetic bounds unattainable by any uniform annulus, while outperforming coordinate-warped lattices that divert axial column thrust into compliant bending paths—thereby complementing density-based and multiscale metamaterial cloaking frameworks [21, 25].

Our fiber-limit theory and 25-dimensional operator spectral diagnostics explain how boundary-trained cloaks develop directional amplification and expose the fundamental limits of strict debiasing. Outer-edge shear stiffening drives soft-mode amplification above the universal geometric threshold $\xi \approx 1.2$ (where $(r-1)/(r_\infty(k)-1) \approx 1 - 1.25/\xi$ collapses aspect ratios across $H/a \in \{2.5, 3.5, 5\}$), enabling zero-optimization bias prediction within 1.3× across seven of eight topologies from intact elastic constants alone (Fig. 6). Moreover, even when a 45°-rotated square plate appears superior under unconstrained uniaxial platen loading (J_{raw} = 0.381 vs. 0.546 at 0°), enforcing soft-mode debiasing erases that advantage completely (+59% penalty to 0.606), proving that orientation gain was driven by unexcited soft-mode amplification rather than intrinsic load shielding. The sole exception—Archimedean 4.8.8—establishes a general physical mechanism: when high Poisson coupling creates substantial bare-hole visibility along a deviatoric soft mode (4.05%), frictionless uniaxial platen training alone self-suppresses bias ($r_s = 0.619$) without needing mixed clamping. Conversely, in sparse aligned square lattices ($\overline{\rho} = 0.25$, λ = 99.7), enforcing strict debiasing redistributes spectral energy across the 25-dimensional basis, halving worst incremental error while shrinking random-load pass rates from 60.4% to 5.2% (Fig. 7c). Intermediate shear constraints (s = 1.5–2) therefore strike a far better structural compromise than rigid unbiasedness when axial loading dominates.

These scaling laws translate directly into three actionable design rules without repeating expensive large-scale topology optimization: (i) size annular inserts to satisfy the equal-mass packing bound $r_{cloak} \gtrsim 1.6\, r_{void}$ (Fig. 5a), beyond which cloaking gains saturate over one shear-lag length $\Lambda_{min} \approx 2.4\, \ell$ and a condensed 36-entry lookup table recovers 54–82% of re-optimized performance in one step (Fig. 5b, c); (ii) select low-λ architectures such as triangular ($\lambda \approx 3-4$) or braced-square grids (≈ 4.2) whenever isotropic shear neutrality takes priority over uniaxial reaction matching; and (iii) audit every mechanical cloaking claim under explicitly declared load subspaces, outer domain cutoffs, and displacement versus strain-energy norms (Fig. 7d).

Several methodological boundaries circumscribe the present framework. All benchmarks assume quasi-static linear elasticity and yield local optima under the specified SLS minimum-feature and clearance limits; three-dimensional unit-cell simulations bracket finite-thickness modulus increases (+3.5% axial and +13% shear, lowering λ by ~8%), while plane-strain idealization shifts baseline raw platen ratio modestly from 0.546 to 0.599 (Supplementary Note 1 and Supplementary Table S2). Moreover, Equation (5) and Table S7 apply specifically to the square-lattice family studied here, and continuation stalls at relative density 0.45 where stocky struts violate slender-beam adjoint assumptions [39]. While linear buckling audits (0.72% out-of-plane critical strain vs. 29–48% in-plane bifurcation), stress-concentration bounds, and 40 stochastic width-scatter realizations up to $\sigma_b = 0.08$mm define the elastic printability and imperfection-tolerance envelope (Supplementary Notes 1–2), full-field experimental testing under controlled platen restraint remains a valuable direction for future work.

Methods

Specimens and platen training set

The reference background structure is a regular square lattice with cell pitch $\ell = L/31 = 4.84$mm filling a $150\text{mm} \times 150\text{mm}$ plate at relative density $\overline{\rho} = 0.35$ (reference uniform strut width $b_{ref} = 0.938$mm, plate half-width $H = L/2$ = 75 mm), with a lattice node positioned at the plate center (Fig. 2a). Around a central circular

cutout of radius $a \equiv r_{\mathrm{void}} = 30\mathrm{mm}$ (6.2 ℓ), width optimization is restricted to the annular insert $\Omega_c = \{r: r_{\mathrm{void}} < r < r_{\mathrm{cloak}}\}$ with outer radius $r_{\mathrm{cloak}} = 55\mathrm{mm}$. Three specimens share identical exterior meshes: (i) intact reference (REF, solid area $A_{\mathrm{REF}} = \overline{\rho} L^2 = 7875\mathrm{mm}^2$); (ii) unreinforced void (VOID, all struts inside r_{void} removed and struts in Ω_c held at b_{ref}); and (iii) mass-neutral cloak (CLOAK, struts inside Ω_c spatially graded while preserving $A(\boldsymbol{x}) = A_{\mathrm{REF}}$). Five multi-topology backgrounds (triangular, honeycomb, braced square, and two square densities; minor clearance adjustments documented in Supplementary Note 3) and the three periodic Laguerre tessellations L1, L2, and L3 use the same outer domain and relative-density conventions.

The constituent polymer is modeled as isotropic linear elastic ($E_s = 1200\mathrm{MPa}$, $\nu_s = 0.35$). The optimization training set $\mathcal{L}_0$ consists of four uniaxial compression load cases applied along either principal plate axis through rigid-elastic 5 mm end platens at 1% nominal strain (tangential platen motion free under frictionless compression and constrained under bonded compression; lateral edges traction-free). Because the governing system is linear, all normalized field and reaction ratios are independent of strain amplitude. Stability checks on a four-subdivision Timoshenko frame mesh with geometric stiffness yield in-plane bifurcation strains of 29–48% across competing square designs and a pinned-end out-of-plane Euler estimate of 0.72% for a 15 mm thick plate (Supplementary Note 1).

Transparency metrics

Exterior nodal displacements $\boldsymbol{u}_X^{(k)}$ ($X \in \{\mathrm{REF}, \mathrm{VOID}, \mathrm{CLOAK}\}$) outside the cloak are interpolated via a fixed linear triangulation onto $N = 122{,}728$ uniform probe points spanning the observation domain $\Gamma = \{r \geq r_{\mathrm{cloak}} + 0.5\mathrm{mm}\}$. Rigid-body translation c and in-plane rotation ω are projected out in least squares via $\mathcal{P}$:

$$\mathcal{P}\,\Delta\boldsymbol{u} = \Delta\boldsymbol{u} - (\boldsymbol{c} + \omega\,\boldsymbol{e}_z \times \boldsymbol{x}), \quad (\boldsymbol{c}, \omega) = \operatorname{argmin} \sum_{i \in \Gamma} |\Delta\boldsymbol{u}_i - \boldsymbol{c} - \omega\,\boldsymbol{e}_z \times \boldsymbol{x}_i|^2 \tag{10}$$

The primary exterior field ratio J is defined as the worst-case relative L_2 mismatch across $\mathcal{L}_0$:

$$J = \max_{k \in \mathcal{L}_0} \frac{\|\mathcal{P}(\boldsymbol{u}_{\mathrm{CLOAK}}^{(k)} - \boldsymbol{u}_{\mathrm{REF}}^{(k)})\|_\Gamma}{\|\mathcal{P}(\boldsymbol{u}_{\mathrm{VOID}}^{(k)} - \boldsymbol{u}_{\mathrm{REF}}^{(k)})\|_\Gamma} \tag{11}$$

where $J = 1$ matches bare-hole visibility and $J = 0$ corresponds to exact exterior invisibility. Because gradient optimization minimizes the unprojected raw ratio J_{raw}, both raw and projected (J) metrics are reported throughout Table 1 and Supplementary Tables S1–S16. Companion indicators measure resultant platen reaction mismatch J_R and far-field exterior error over $\Gamma_{\mathrm{far}} = \{r \geq r_{\mathrm{cloak}} + 10.5\mathrm{mm}\}$.

Beam and continuum mechanical models

Optimization gradients are evaluated rapidly on a Timoshenko beam surrogate discretizing each strut into seven collinear segments with shear correction factor 5/6 (and on an Euler–Bernoulli surrogate during initial 9-family screening; Supplementary Fig. S1a). All final reported field ratios, reaction forces, unseen-load benchmarks, and operator spectra are verified directly on a high-resolution plane-stress continuum grid of Wilson Q6 incompatible-mode elements [46] integrated with 8 × 8 subpixel Gauss quadrature across exact rounded strut junctions and 5 mm solid end bars. Primary platen evaluations use grid step $h = 0.05\mathrm{mm}$ (3,000 × 3,000 elements), while mesh-refinement invariance down to h = 0.0375 mm, plane-stress versus plane-strain comparisons, and 3D hexahedral unit-cell benchmarks (0.12 mm in-plane, 0.25 mm half-thickness step) are documented in Supplementary Note 1 and Supplementary Tables S1a–b, S2.

Design parametrization and fabrication bounds

Keeping all nodal connectivity fixed within the ≈ 1,760-member plate, the baseline square cloak contains 500 active design members with independent mid-span widths b_m and 484 tapered struts (>2 mm length, excluding 16

short rim stubs) with independent joint-neck widths b_e. Each tapered strut assigns b_e over the outer 25% at both ends, transitions linearly across 10%, and holds b_m over the central 30%. Because strut bending stiffness scales as b^3 while axial stiffness scales as b, neck tapering ($b_e < b_m$) selectively decouples joint shear compliance from axial load transfer. Respecting SLS polymer additive-manufacturing constraints [26, 40], all variables satisfy $0.5\text{mm} \le b_m, b_e \le 2.0\text{mm}$, minimum clear gap $\ge 0.5\text{mm}$, and minimum straight segment length $\ge 1.0\text{mm}$.

Multi-fidelity trust-region optimization and shear control

Collecting all width variables in x, the constrained mass-neutral problem

$$\min_{\boldsymbol{x}} J_{\text{raw}}(\boldsymbol{x}) \ \text{s.t.}\ A(\boldsymbol{x}) = A_{\text{REF}}, \quad b_{\min} \le x_j \le b_{\max}, \quad g(\boldsymbol{x}) \ge g_{\min} \tag{12}$$

is solved via a five-step surrogate-managed trust-region algorithm [47]: (i) add continuum-minus-beam residual shifts $\boldsymbol{D}_k = \boldsymbol{e}_k^{\text{cont}}(\boldsymbol{x}_c) - \boldsymbol{e}_k^{\text{beam}}(\boldsymbol{x}_c)$ while keeping analytical beam adjoint gradients; (ii) aggregate minimax objectives via smooth Kreisselmeier–Steinhauser continuation $J_{\text{KS}} = J_{\max} + \beta^{-1}\ln\sum_k \exp[\beta(J_k - J_{\max})]$ [48] over $\beta \in \{30,100,300\}/J$; (iii) execute 35 spectral projected-gradient iterations (SPG2 [49]) within box bounds, trust radius $\|\boldsymbol{x} - \boldsymbol{x}_c\|_\infty \le \Delta$, and linearized area conservation; (iv) enforce exact Boolean solid-area closure via Illinois regula falsi until $|A(\boldsymbol{x}) - A_{\text{REF}}|/A_{\text{REF}} \le 10^{-4}$; and (v) accept steps reducing continuum J with adaptive $\Delta \in [0.01,0.35]\text{mm}$ (initial $\Delta_0 = 0.12\text{mm}$). Ten outer passes from uniform b_{ref} yield the baseline Graded cloak, while an alternative displacement-loaded initialization (Warm-start) assesses local-minimum sensitivity (Supplementary Note 1). Neither unseen loads nor stochastic scatter enter the optimization objective. For explicit shear control, either the minimax epigraph objective $\min\max(J, r_\gamma/s)$ ($s \in \{2, 1.5, 1\}$) or bounded soft-mode continuation $r_s \le 1.02$ (1–3 continuation passes) is added cleanly.

Stochastic width scatter and full-space 25D operator analysis

Manufacturing imperfection sensitivity [40, 41] is probed using spatially correlated random width fields $\delta b(\boldsymbol{x}_e) = \sigma_b f(\boldsymbol{x}_e)$ (20 mm correlation length constructed from 400 Fourier modes) applied identically to REF, VOID, and CLOAK across 10 paired continuum prints at $\sigma_b = 0.06\text{mm}$ and extended 40-realization marker sweeps up to $\sigma_b = 0.08\text{mm}$ (Supplementary Note 2 and Supplementary Table S5). Generalization across the complete 25-dimensional fourth-order polynomial boundary-displacement basis is audited without subspace truncation via Equation (9), where $\boldsymbol{G}_R$ is the protocol-matched intact reference Gram matrix and $h_{\max} = 10^4\eta_{\max}(\boldsymbol{Q}_W, \boldsymbol{G}_R)$ measures worst incremental excess error in $\%^2$. Five nested protocols isolate rigid-body projection, inner versus outer cutoff radius ($r \ge 55.5$ mm vs. 58.0 mm, 245k DOFs vs. 301k–477k elements), and L_2 displacement versus elementwise Q6 strain-energy norms, paired with 2,000 standard-normal Gaussian boundary-load draws (Supplementary Note 4 and Supplementary Tables S14–S16).

Lekhnitskii anisotropic dipole derivation

Consider an infinite orthotropic sheet with compliances $a_{11} = a_{22} = 1/E$, $a_{12} = -\nu/E$, and $a_{66} = 1/G$ perforated by a circular hole of radius a. Complex Lekhnitskii potentials $\Phi_k(z_k)$ ($z_k = x + \mu_k y$, $\mu_k = i\beta_k$, $\beta_1\beta_2 = 1$, satisfying $\mu^4 + (\kappa - 2\nu)\mu^2 + 1 = 0$) [35] are mapped conformally onto ζ_k with exterior dipole perturbation $\Phi_k = C_k/\zeta_k$. For $\nu = 0, a = 1, \Delta = \beta_2 - \beta_1$, remote uniaxial tension $\sigma_y = 1$ gives $C_1 = -\beta_2/(2\Delta)$ and $C_2 = \beta_1/(2\Delta)$, whereas remote pure shear $\tau_{xy} = \tau$ gives $C_1 = i\tau(1 + \beta_2)/(2\Delta)$ and $C_2 = -i\tau(1 + \beta_1)/(2\Delta)$. Leading far-field dipole coefficients D_k/z_k ($D_k = C_k(1 + \beta_k)/2$) satisfy exact angular residue averages over $w_k(\theta) = 1/(\cos\theta + i\beta_k\sin\theta)$ (zero cross-mean $w_j w_k = 0$ and conjugate mean $w_j\overline{w}_k = 2/(\beta_j + \beta_k)$). Setting $\beta_1 + \beta_2 = q = \sqrt{\kappa + 2}$ recovers Equation (2) exactly, matching numerical quadrature to four digits and finite-plate Q6 continuum ratios within 15%. Retaining nonzero ν yields the full dipole values quoted in Results.

Effective stiffness of the lattice network library

From 63 candidate periodic/Archimedean tilings [36] and disordered Laguerre Voronoi cellular networks [37, 38], 41 candidates failing connectivity or clearance checks are removed, leaving 22 connected periodic graphs. Following energy-based homogenization [50], each intact lattice's stiffness tensor $\boldsymbol{C}$ is extracted from three 1% uniform-strain beam solutions ($\varepsilon_{xx}, \varepsilon_{yy}, \gamma_{xy}$ with free nodal rotations) over a central sampling window Ω_w of half-width $l_w = 0.35L$ combining bilinear strain energies $W_{ij} = \boldsymbol{u}_i^{\mathrm{T}} \boldsymbol{K}_W \boldsymbol{u}_j$ with best-fit interior affine strain $\overline{\boldsymbol{\varepsilon}}$:

$$\boldsymbol{C} = \frac{1}{A_W}\, \overline{\boldsymbol{\varepsilon}}^{-\mathrm{T}}\, \boldsymbol{W}\, \overline{\boldsymbol{\varepsilon}}^{-1} \tag{13}$$

Evaluating Equation (13) on best-fit interior strain eliminates boundary-layer edge artifacts, bringing isotropic networks within 5–8% of theoretical $\kappa = 2(1+\nu)$ (vs. 15–21% using global boundary strain). Applying the non-affine exclusion gate $\|\overline{\boldsymbol{\varepsilon}}\boldsymbol{\varepsilon}^{-1} - \boldsymbol{I}\| > 0.5$ cleanly flags and removes three outliers exhibiting 82–97% interior strain departure (Supplementary Fig. S9 and Supplementary Table S19), yielding the 19 homogenizable backgrounds in Fig. 1.

Data availability

All benchmark numerical datasets—including continuum mesh-convergence tests, manufacturing-scatter Monte Carlo outputs, competing-architecture tables, scale-transfer benchmarks, full 25-dimensional operator spectra, eight-topology homogenized constants, and the complete 22-network lattice stiffness library—are provided in the Supplementary Information (Supplementary Tables S1–S19) and accompanying CSV datasets (graded_cloak_36_entry_lookup_table.csv, lattice_library_22_networks_full_C.csv, and lattice_library_63_screening_log.csv) deposited with the submission archive. Permanent repository DOIs will be provided upon publication.

Code availability

The MATLAB and Python simulation codes implementing Timoshenko frame optimization, Wilson Q6 continuum verification, boolean area closure, 25-dimensional fourth-order operator spectral auditing, and figure generation are included in the submission archive (uglc_core_matlab and reproduction scripts) for peer review and will be publicly released upon publication.

References

1. Kirsch, G. Die Theorie der Elastizität und die Bedürfnisse der Festigkeitslehre. *Z. Ver. Dtsch. Ing.* **42**, 797–807 (1898).

2. Savin, G. N. Stress Concentration Around Holes. (Pergamon Press, Oxford, 1961).

3. Mansfield, E. H. Neutral holes in plane sheet — reinforced holes which are elastically equivalent to the uncut sheet. *Q. J. Mech. Appl. Math.* **6**, 370–378 (1953).

4. Milton, G. W. & Serkov, S. K. Neutral coated inclusions in conductivity and anti-plane elasticity. *Proc. R. Soc. Lond. A* **457**, 1973–1997 (2001).

5. Milton, G. W. The Theory of Composites. (Cambridge Univ. Press, Cambridge, 2002).

6. Norris, A. N. & Parnell, W. J. Static elastic cloaking, low-frequency elastic wave transparency and neutral inclusions. *Proc. R. Soc. A* **476**, 20190725 (2020).

7. Pendry, J. B., Schurig, D. & Smith, D. R. Controlling electromagnetic fields. *Science* **312**, 1780–1782 (2006).

8. Milton, G. W., Briane, M. & Willis, J. R. On cloaking for elasticity and physical equations with a transformation invariant form. *New J. Phys.* **8**, 248 (2006).

9. Norris, A. N. & Shuvalov, A. L. Elastic cloaking theory. *Wave Motion* **48**, 525–538 (2011).

10. Brun, M., Guenneau, S. & Movchan, A. B. Achieving control of in-plane elastic waves. *Appl. Phys. Lett.* **94**, 061903 (2009).

11. Farhat, M., Guenneau, S. & Enoch, S. Ultrabroadband elastic cloaking in thin plates. *Phys. Rev. Lett.* **103**, 024301 (2009).

12. Stenger, N., Wilhelm, M. & Wegener, M. Experiments on elastic cloaking in thin plates. *Phys. Rev. Lett.* **108**, 014301 (2012).

13. Milton, G. W. & Cherkaev, A. V. Which elasticity tensors are realizable?. *J. Eng. Mater. Technol.* **117**, 483–493 (1995).

14. Bückmann, T., Thiel, M., Kadic, M., Schittny, R. & Wegener, M. An elasto-mechanical unfeelability cloak made of pentamode metamaterials. *Nat. Commun.* **5**, 4130 (2014).

15. Hai, L., Zhao, Q. & Meng, Y. Unfeelable mechanical cloak based on proportional parameter transform in bimode structures. *Adv. Funct. Mater.* **28**, 1801473 (2018).

16. Kadic, M., Milton, G. W., van Hecke, M. & Wegener, M. 3D metamaterials. *Nat. Rev. Phys.* **1**, 198–210 (2019).

17. Bückmann, T., Kadic, M., Schittny, R. & Wegener, M. Mechanical cloak design by direct lattice transformation. *Proc. Natl. Acad. Sci. U.S.A.* **112**, 4930–4934 (2015).

18. Kadic, M. et al. Elastodynamic behavior of mechanical cloaks designed by direct lattice transformations. *Wave Motion* **92**, 102419 (2020).

19. Bendsøe, M. P. & Sigmund, O. Topology Optimization: Theory, Methods, and Applications. (Springer, Berlin, 2003).

20. Sigmund, O. & Maute, K. Topology optimization approaches: a comparative review. *Struct. Multidiscip. Optim.* **48**, 1031–1055 (2013).

21. Sanders, E. D., Aguiló, M. A. & Paulino, G. H. Optimized lattice-based metamaterials for elastostatic cloaking. *Proc. R. Soc. A* **477**, 20210418 (2021).

22. Wang, L. et al. Mechanical cloak via data-driven aperiodic metamaterial design. *Proc. Natl. Acad. Sci. U.S.A.* **119**, e2122185119 (2022).

23. Cheng, X. et al. A compatible boundary condition-based topology optimization paradigm for static mechanical cloak design. *Extreme Mech. Lett.* **65**, 102100 (2023).

24. Lu, Y. & Tong, L. Concurrent multiscale topology optimization of metamaterials for mechanical cloak. *Comput. Methods Appl. Mech. Eng.* **409**, 115966 (2023).

25. Sozio, F., Shojaei, M. F. & Yavari, A. Optimal elastostatic cloaks. *J. Mech. Phys. Solids* **176**, 105306 (2023).

26. Yang, Z. et al. Static mechanical cloaking and camouflage from disorder. *Nat. Commun.* **16**, 8858 (2025).

27. Senhora, F. V., Sanders, E. D. & Paulino, G. H. Unbiased mechanical cloaks. *Proc. Natl. Acad. Sci. U.S.A.* **122**, e2415056122 (2025).

28. Gibson, L. J. & Ashby, M. F. Cellular Solids: Structure and Properties 2nd edn. (Cambridge Univ. Press, Cambridge, 1997).

29. Fleck, N. A., Deshpande, V. S. & Ashby, M. F. Micro-architectured materials: past, present and future. *Proc. R. Soc. A* **466**, 2495–2516 (2010).

30. Schaedler, T. A. & Carter, W. B. Architected cellular materials. *Annu. Rev. Mater. Res.* **46**, 187–210 (2016).

31. Maxwell, J. C. On the calculation of the equilibrium and stiffness of frames. *Philos. Mag.* **27**, 294–299 (1864).

32. Berger, J. B., Wadley, H. N. G. & McMeeking, R. M. Mechanical metamaterials at the theoretical limit of isotropic elastic stiffness. *Nature* **543**, 533–537 (2017).

33. Deshpande, V. S., Ashby, M. F. & Fleck, N. A. Foam topology: bending versus stretching dominated architectures. *Acta Mater.* **49**, 1035–1040 (2001).

34. Wang, A.-J. & McDowell, D. L. In-plane stiffness and yield strength of periodic metal honeycombs. *J. Eng. Mater. Technol.* **126**, 137–156 (2004).

35. Lekhnitskii, S. G. Anisotropic Plates. (Gordon and Breach, New York, 1968).

36. Grünbaum, B. & Shephard, G. C. Tilings and Patterns. (W. H. Freeman, New York, 1987).

37. Bhuwal, A. S., Pang, Y., Ashcroft, I., Sun, W. & Liu, T. Discovery of quasi-disordered truss metamaterials inspired by natural cellular materials. *J. Mech. Phys. Solids* **175**, 105294 (2023).

38. Luan, S., Chen, E., John, J. & Gaitanaros, S. A data-driven framework for structure–property correlation in ordered and disordered cellular metamaterials. *Sci. Adv.* **9**, eadi1453 (2023).

39. Portela, C. M., Greer, J. R. & Kochmann, D. M. Impact of node geometry on the effective stiffness of non-slender three-dimensional truss lattice architectures. *Extreme Mech. Lett.* **22**, 138–148 (2018).

40. Benedetti, M. et al. Architected cellular materials: a review on their mechanical properties towards fatigue-tolerant design and fabrication. *Mater. Sci. Eng. R Rep.* **144**, 100606 (2021).

41. Gross, A., Pantidis, P., Bertoldi, K. & Gerasimidis, S. Correlation between topology and elastic properties of imperfect truss-lattice materials. *J. Mech. Phys. Solids* **124**, 577–598 (2019).

42. Cox, H. L. The elasticity and strength of paper and other fibrous materials. *Br. J. Appl. Phys.* **3**, 72–79 (1952).

43. Choi, I. & Horgan, C. O. Saint-Venant's principle and end effects in anisotropic elasticity. *J. Appl. Mech.* **44**, 424–430 (1977).

44. Horgan, C. O. Saint-Venant end effects in composites. *J. Compos. Mater.* **16**, 411–422 (1982).

45. Mehrabadi, M. M. & Cowin, S. C. Eigentensors of linear anisotropic elastic materials. *Q. J. Mech. Appl. Math.* **43**, 15–41 (1990).

46. Wilson, E. L., Taylor, R. L., Doherty, W. P. & Ghaboussi, J. Incompatible displacement models. in Numerical and Computer Methods in Structural Mechanics (eds Fenves, S. J., Perrone, N., Robinson, A. R. & Schnobrich, W. C.) 43–57 (Academic Press, New York) (1973).

47. Alexandrov, N. M., Dennis, J. E., Lewis, R. M. & Torczon, V. A trust-region framework for managing the use of approximation models in optimization. *Struct. Optim.* **15**, 16–23 (1998).

48. Kreisselmeier, G. & Steinhauser, R. Systematic control design by optimizing a vector performance index. in Computer Aided Design of Control Systems (ed. Cuénod, M. A.) 113–117 (Pergamon) (1979).

49. Birgin, E. G., Martínez, J. M. & Raydan, M. Nonmonotone spectral projected gradient methods on convex sets. *SIAM J. Optim.* **10**, 1196–1211 (2000).

50. Hill, R. Elastic properties of reinforced solids: some theoretical principles. *J. Mech. Phys. Solids* **11**, 357–372 (1963).

Acknowledgements

This work was supported by the Fujian Provincial Health Technology Project (Grant No. 2024GGA052).

Author contributions

G.W. conceived the study, developed the methodology, wrote the optimization and continuum verification software, performed formal analysis, curated the datasets, visualized the results, and wrote the original draft. M.Y. contributed to software implementation, numerical investigation, and validation. J.L. contributed to conceptualization, funding acquisition, and project administration. All authors reviewed and approved the final manuscript.

Competing interests

The authors declare no competing interests.